ACS APPLIED ELECTRONIC MATERIALS

pubs.acs.org/acsaelm Article

High-Performance Ammonia Plasma-Processed $CsPbBr_3$ Perovskite Photodetectors

Zewen Lin, Zhenxu Lin, Jie Song, Rui Huang,* Haixia Wu, Kaitao Chen, Li Xia, Yi Zhang, Hongliang Li, Yanqing Guo, Huihong Lin, and Paul K. Chu*

Cite This: *ACS Appl. Electron. Mater.* 2025, 7, 5404−5411 Read Online

ACCESS | Metrics & More | Article Recommendations | Supporting Information

ABSTRACT: The pursuit of defect-suppressed metal halide perovskite films with optimal optoelectronic properties remains a persistent challenge in semiconductor device engineering. In this study, the effects of NH_3 plasma on the fabrication of high-quality $CsPbBr_3$ perovskite films are evaluated systematically. NH_3 plasma generates NH_2 and NH species, which enhance grain growth and reduce defect states. As a result, the trap density decreases significantly from 7.9×10^{12} cm^{-3} to 6.8×10^{11} cm^{-3}, improving $CsPbBr_3$ film quality. The photodetector assembled with the NH_3 plasma-processed $CsPbBr_3$ film delivers outstanding performance, including a responsivity of 62.7 A/W, detectivity of 7.7×10^{12} Jones, ultrafast response time of 0.1/0.3 ms, and exceptional stability, all of which surpass the metrics of the non-plasma-treated device. These findings offer a promising solution for enhancing the quality of $CsPbBr_3$ perovskite films, thereby improving the properties of optoelectronic devices.

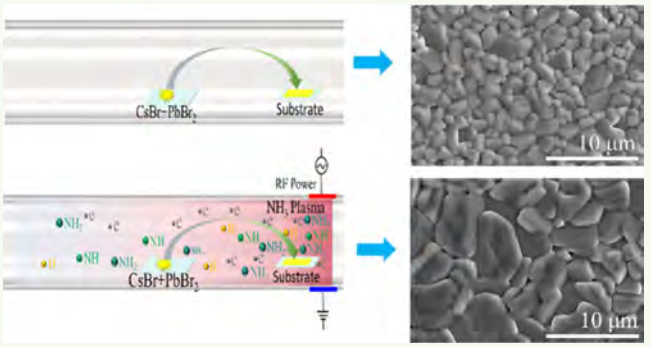

KEYWORDS: *Chemical vapor deposition, $CsPbBr_3$ films, Plasma, NH_3, Photoconductors, Photodetectors.*

1. INTRODUCTION

Lead halide perovskites have attracted significant attention due to their outstanding optoelectronic properties, including high carrier mobility, large absorption coefficients, long carrier diffusion lengths, and high photoluminescence (PL) quantum efficiency.[1−3] These exceptional characteristics make perovskite materials highly promising for a wide range of optoelectronic applications, such as solar cells, photodetectors, light-emitting diodes, and lasers.[4−9] Compared to organic−inorganic hybrid perovskites, all-inorganic perovskite materials like $CsPbBr_3$ have superior stability, rendering them highly promising in optoelectronic devices.[10−15] Nevertheless, despite these advantages, producing high-quality perovskite films is still challenging. These films often contain crystal defects, such as uncoordinated ions and dangling bonds, on the surface and in grain boundaries. These defects can lead to nonradiative charge recombination and reduce the efficiency of optoelectronic devices.[16] Moreover, they can cause ion migration and water exposure, resulting in environmental instability and further degradation of device performance.[17] Therefore, minimizing crystal defects and improving film crystallinity, especially grain size and uniformity, are crucial to enhancing the optoelectronic properties. Various strategies have been proposed to improve the quality of perovskite films, for example, by taking advantage of functional groups with coordination properties to reduce grain boundary defects and promote uniform grain growth.[18−21] In this respect, NH_2 and NH functional groups can coordinate with metal cations such as Pb^{2+} and Sn^{2+} in the precursor solution to lower the reactivity of metal ions, regulate the nucleation rate, and avoid excessively fast or uneven nucleation. These approaches have been demonstrated to slow crystal growth and improve uniformity and crystallinity.[22,23] Specifically, NH_2 functional groups can coordinate with Sn^{2+}/Pb^{2+} to slow crystal growth and enhance the grain size in mixed Sn−Pb perovskites.[23]

Although the use of functional groups is promising in solution-based methods, their application to chemical vapor deposition (CVD) remains largely unexplored. Despite the advantages of CVD such as large-area deposition, films produced by this method, such as $CsPbBr_3$, are typically plagued by low carrier mobility and high defect density.[24,25] It is thus crucial to precisely control the film uniformity and crystal growth directionality during CVD in order to obtain larger grains with a low defect density. It is well established that activation through glow discharge plasma enhances

Received: February 23, 2025
Revised: June 5, 2025
Accepted: June 6, 2025
Published: June 11, 2025

https://doi.org/10.1021/acsaelm.5c00374
ACS Appl. Electron. Mater. 2025, 7, 5404−5411

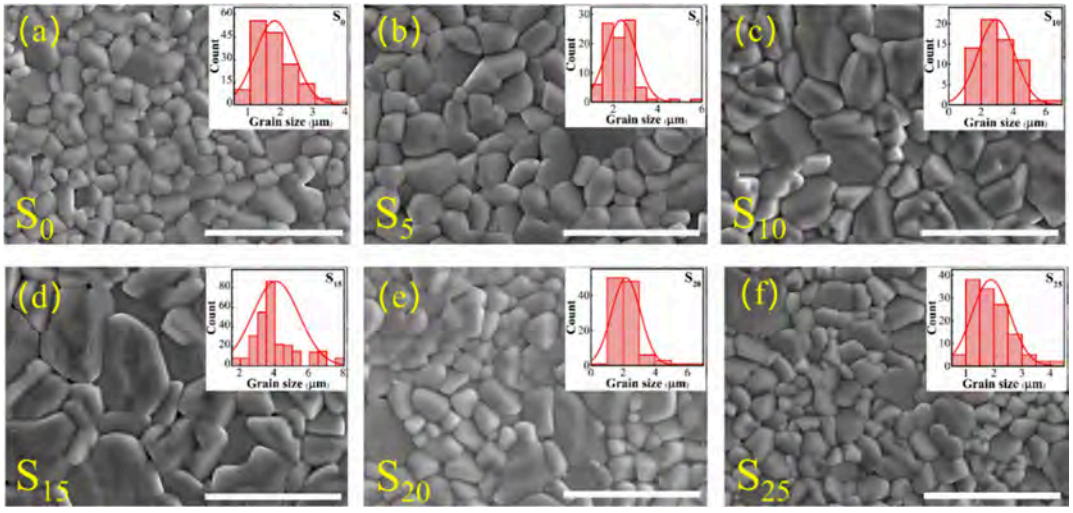

Figure 1. SEM images of the $CsPbBr_3$ films prepared at different NH_3 flow rates: (a) 0, (b) 5, (c) 10, (d) 15, (e) 20, and (f) 25 sccm (scale bar = 5 μm) with the insets showing the grain diameter statistics of the corresponding $CsPbBr_3$ films. The grain sizes were calculated by analyzing over 150 grains from independent SEM images using the Image particle analysis tool.

material reactivity, accelerates surface reactions, and fosters the formation of dense and uniform films with superior properties. However, its application has mainly focused on modifying halide perovskite film surfaces to improve the device performance. In this work, unlike traditional plasma surface modification of halide perovskite films,[26−32] NH_3 plasma processing is combined with CVD to prepare $CsPbBr_3$ films, and the impact of various active species, such as H, NH, and NH_2 generated by the plasma, on the film quality is investigated. The schematic diagram of the experimental setup and flow is presented in Figure S1 (Supporting Information). Our findings reveal that the ammonia plasma not only promotes grain growth and reduces grain boundaries but also mitigates sub-band gap absorption and eliminates defect states in the films. Owing to the superior film quality, the photodetector has exceptional characteristics.

2. MATERIALS AND METHODS

Materials. Cesium bromide (CsBr, 99.9%) and lead(II) bromide ($PbBr_2$, 99.9%) were sourced from Aladdin Corp. (China) and used without further purification.

Preparation of $CsPbBr_3$ Films. The $CsPbBr_3$ films were prepared by one-step plasma-assisted chemical vapor deposition (CVD) in a quartz tube furnace. The $PbBr_2$ (0.05 g) and CsBr (0.05 g) powders were placed in the high-temperature zone, while the silicon-on-insulator (SOI) substrate was positioned in the low-temperature region. The system was evacuated to a base pressure of 0.6 Pa, and argon (40 sccm, 99.9999% purity) and NH_3 (99.9999% purity) were introduced to maintain a working pressure of 90 Pa. The precursors were heated at a rate of 30 °C/min to 630 °C, at which point the glow discharge plasma was ignited with an RF power of 10 W. The NH_3 flow rate was varied between 0 and 25 sccm. The deposition was carried out for 20 min, and afterward, the $CsPbBr_3$ films were naturally cooled to room temperature. The samples, fabricated using different NH_3 flow rates, were labeled as S_X, where X = 0, 5, 10, 15, 20, or 25 represents the corresponding NH_3 flow rate.

Device Fabrication and Photoelectrical Measurements. The planar photodetectors with a metal−semiconductor−metal (MSM) architecture were fabricated by depositing interdigital gold (Au) electrodes with a 50 μm gap by magnetron sputtering by using a custom mask. The schematic structure of the photodetector with a $CsPbBr_3$ film thickness of approximately 2 μm is displayed in Figure S2 (Supporting Information). The electrical and photoelectrical properties of the devices were determined at room temperature using a Keithley 6517B electrometer coupled to a probe station. The photocurrents were measured upon illumination with lasers with wavelengths of 280, 365, 450, 550, 625, and 730 nm. The response time was determined on a Rigol MSO7014 oscilloscope in conjunction with a pulsed 450 nm laser.

Characterization. The surface morphology of the films was examined by scanning electron microscopy (SEM) on a Hitachi SU5000, and microstructural analysis was performed on a Horiba LabRAM HR Evolution Raman spectrometer. The elemental composition was determined by energy-dispersive X-ray spectroscopy (EDS) using a Bruker EDS QUANTAX system. The photoluminescence (PL) and time-resolved PL measurements were carried out on an Edinburgh FLS1000. The crystal structure was analyzed by X-ray diffraction (XRD) performed on the X'pertPro Panalytical diffractometer, and the UV−vis absorption spectra were acquired on the Shimadzu UV-3600 spectrophotometer.

3. RESULT AND DISCUSSION

The samples fabricated under plasma conditions and using different ammonia gas flow rates exhibit a pronounced Raman peak at 70 cm^{-1} and a broad band at 125 cm^{-1} (Figure S3, Supporting Information), both of which are typical lattice vibration modes of $CsPbBr_3$ associated with the vibration of $[PbBr_6]^{4-}$ octahedra and motion of Cs^+, respectively, while the peak at 311 cm^{-1} is related to the Raman second-order phonon scattering mode of $CsPbBr_3$.[33] Figures 1a to 1f present the SEM images of the samples prepared under plasma conditions and using different ammonia flow rates. In the absence of ammonia plasma, the surface morphology of the sample is dense, with grain sizes of approximately 2.0 μm. After exposure to ammonia plasma, a noticeable increase in the primary grain size is observed. At an ammonia flow rate of 15 sccm, the grain size increased significantly to about 4.0 μm. Concurrently, the grain density decreases with increasing ammonia flow rates, showing a significant reduction in grain boundaries. However, when the ammonia gas flow rate increases further from 15 to 25 sccm, the grain size decreases gradually and the grain density increases. The results indicate that within a certain range, a moderately higher flow rate of ammonia facilitates grain growth and reduces the number of grain boundaries. Figure S4 (Supporting Information) displays the X-ray diffraction (XRD) patterns of the samples, which exhibit a

https://doi.org/10.1021/acsaelm.5c00374
ACS Appl. Electron. Mater. 2025, 7, 5404−5411

polycrystalline cubic perovskite structure (PDF#54-0752) with *Pm*3*m* symmetry. The diffraction peaks at 21.6° and 26.6°, corresponding to the (110) and (211) planes of $CsPbBr_3$, are prominent. As the ammonia flow rate increases, the intensity of the (110) peak becomes higher, suggesting that a higher ammonia flow favors preferential growth along the (110) direction. Hence, the NH_3 plasma plays an important role in the deposition of $CsPbBr_3$ films similar to that of NH_2 and NH functional groups in solution-based methods.

The samples exhibit a primary absorption edge near 2.3 eV (Figure 2), consistent with the typical absorption profile of $CsPbBr_3$.[34] Significant sub-band gap absorption is observed in the range of 1.7−2.2 eV due to defect states, which introduce localized energy levels that facilitate electron transitions and allow absorption of low-energy photons. As the NH_3 flow rate is increased to 15 sccm, a substantial reduction in sub-band gap absorption is observed, suggesting that the higher NH_3 flow rate reduces the density of defect states. However, when the NH_3 flow rate is excessively high, sub-band gap absorption increases once again, signaling the formation of additional low-energy states. The variation in sub-band gap absorption with increasing NH_3 flow rate is consistent with the trend observed in Urbach energy evolution (Figure S5, Supporting Information). Therefore, an excessively high NH_3 flow rate may produce structural disorder and increase the defect state density, potentially linked to the proliferation of grain boundaries, as shown in the SEM images in Figure 1. The PL characteristics of the films are shown in Figure 3a. All samples exhibit a characteristic emission peak around 530 nm typical of $CsPbBr_3$.[34] The PL intensity depends on the NH_3 flow rate, increasing sharply with the NH_3 flow rate and reaching a maximum at 15 sccm. This observation suggests a substantial decrease in nonradiative recombination centers as the NH_3 flow rate increases to 15 sccm. However, a further increase in the NH_3 flow rate decreases the PL intensity, indicating that the optimal NH_3 flow rate is necessary to reduce nonradiative recombination centers and suppress nonradiative recombination. In fact, beyond the optimal flow rate, excessive plasma exposure may induce surface damage or etching effects and then introduce additional surface or bulk defects, thereby leading to a decrease in PL intensity. The correlation between PL intensity and NH_3 flow rate aligns with the relationship between changes in sub-band gap absorption and NH_3 flow rate, consequently supporting the conclusion

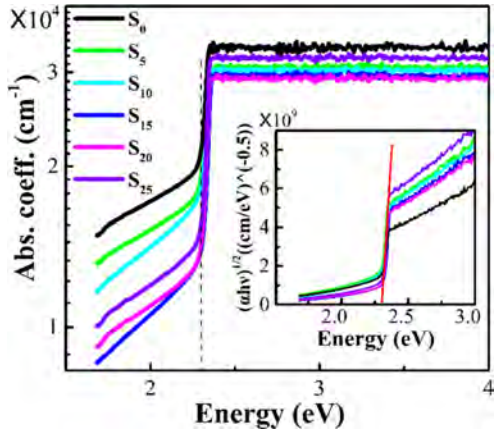

Figure 2. Optical absorption spectra of the $CsPbBr_3$ films prepared at different NH_3 flow rates with the inset showing the Tauc plots of the $CsPbBr_3$ films derived from the absorption spectra.[35]

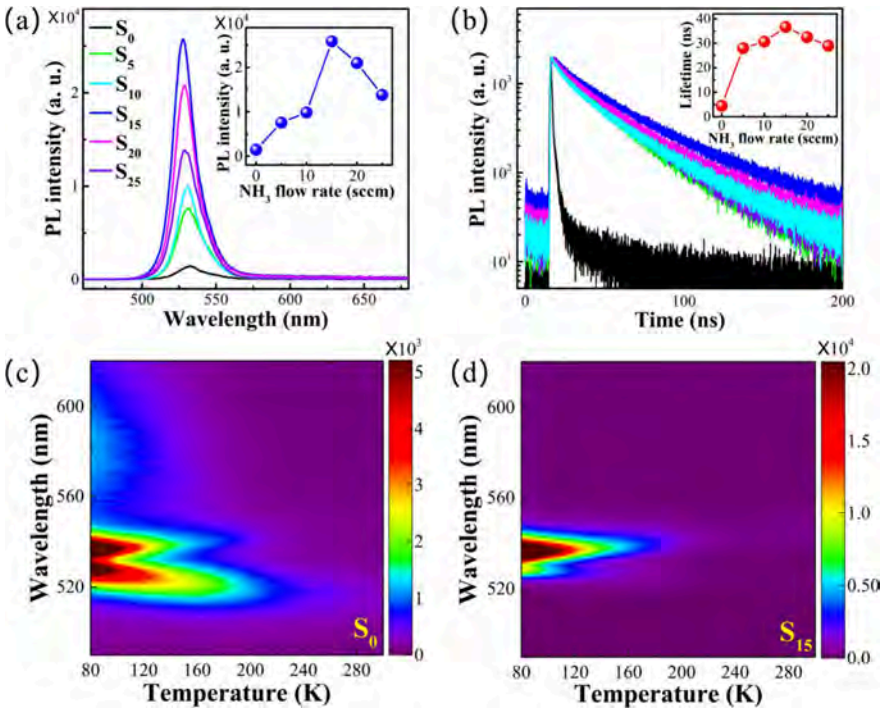

Figure 3. (a) PL spectra of $CsPbBr_3$ films deposited at different NH_3 flow rates excited by the 375 nm Xe lamp with the inset showing the PL intensity as a function of NH_3 flow rates; (b) TRPL spectra of $CsPbBr_3$ films prepared at different NH_3 flow rates monitored at 540 nm with the inset showing the PL lifetime as a function of NH_3 flow rates; 2D pseudocolor maps of the PL spectra as a function of temperature from 80 to 300 K of the $CsPbBr_3$ films prepared (c) without and (d) with NH_3 plasma at a flow rate of 15 sccm.

https://doi.org/10.1021/acsaelm.5c00374
ACS Appl. Electron. Mater. 2025, 7, 5404−5411

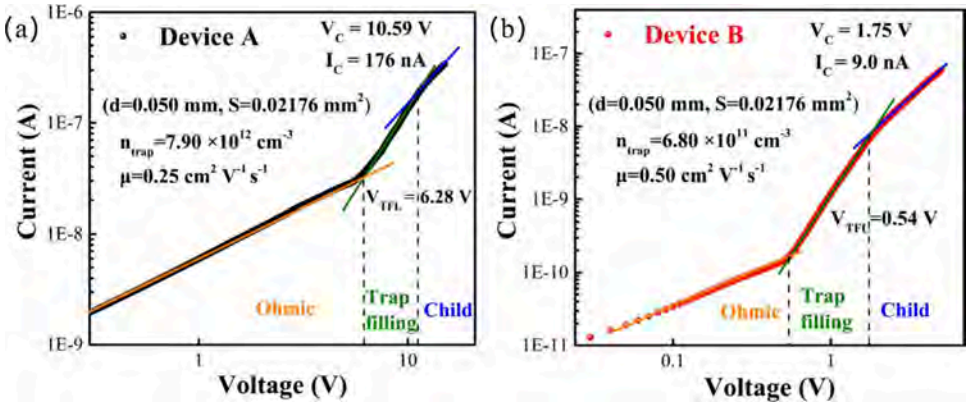

Figure 4. SCLC measurements of the $CsPbBr_3$ films prepared (a) without and (b) with NH_3 plasma at a flow rate of 15 sccm.

that an appropriate NH_3 plasma flow rate can reduce the defect state density in the films, while an excessively high NH_3 flow rate increases the defect state density. Figure 3(b) presents the PL decay curves of the samples processed under varying NH_3 flow rates. The PL decay can be fitted by the following biexponential function:[36]

$$I(t) = I_0 + A_1 e^{-t/\tau 1} + A_2 e^{-t/\tau 2} \quad (1)$$

where I_0 represents the background level, τ_1 and τ_2 are the fast and slow decay time constants, and A_1 and A_2 are the corresponding amplitudes. The average PL lifetime was calculated as described in ref 36, increases from 4.5 to 36.6 ns as the NH_3 flow rate increases from 0 to 15 sccm (inset in Figure 3b), indicating a significant reduction in nonradiative recombination centers in the films grown with the NH_3 plasma. However, further increasing the NH_3 flow rate from 15 to 25 sccm results in a slight reduction in the PL lifetime to 29 ns due to the introduction of additional defect states, as discussed above. Figures 3c and 3d present the 2D pseudo-color maps of the temperature-dependent PL spectra of the $CsPbBr_3$ films, revealing a consistent blue shift as the temperature decreases from 300 to 80 K, accompanied by a notable narrowing of the full-width at half-maximum (fwhm) of the PL peaks. As the temperature decreases to 80 K, amplified spontaneous emission (ASE) at around 540 nm with a fwhm of approximately 7 nm becomes prominent in both samples. However, with regard to the sample prepared without the NH_3 plasma, a broad and weak emission band associated with self-trapped excitons (STEs) is observed in the 550−650 nm region with a peak at 570 nm.[37] The intensity of this emission band increases as the temperature decreases. In contrast, this self-trapped exciton emission peak is absent from the sample prepared with 15 sccm of NH_3, demonstrating the effective elimination of defect states in the film.

To further evaluate the quality of the $CsPbBr_3$ films, we employed the space-charge-limited current (SCLC) method, a well-established technique for probing charge transport characteristics such as trap density and carrier mobility in semiconducting thin films.[38] The measurements were carried out on single-carrier devices with a sandwich architecture in which charge transport is dominated by a single carrier type. The current−voltage (I−V) characteristics obtained from these devices were used to extract quantitative information on defect states and carrier dynamics. Figure 4 reveals three distinct regions. The ohmic region (n = 1, orange line) is observed at a low bias, followed by the trap-filled region (n > 3, green line) starting at trap-filled limit voltage (V_{TFL}), where all of the traps are filled. At a high bias, the Child region (n = 2, blue line) is observed. Notably, after NH_3 plasma processing, the V_{TFL} diminishes to approximately 0.54 V, compared to 6.28 V for the untreated film. The defect density (n_{trap}) and charge carrier mobility (μ) can be derived by the Mott−Gurney equation:[38]

$$n_{trap} = \frac{2\varepsilon_0 \varepsilon_r V_{TFL}}{eL^2} \quad (2)$$

$$\mu = \frac{8JL^3}{9\varepsilon_0 \varepsilon_r V^2} \quad (3)$$

where e represents the elementary charge, ε_0 is the vacuum permittivity, ε_r is the relative dielectric constant, L represents the 50 μm separation between the electrodes, and V and J are the Child limit voltage and the corresponding current density, respectively. The defect density of the NH_3 plasma-processed film is determined to be 6.8 × 10^{11} cm^{-3}, revealing a substantial decrease from 7.9 × 10^{12} cm^{-3} of the untreated films. The reduction in defect states highlights the effectiveness of NH_3 plasma in enhancing the film quality. The charge carrier mobility of the plasma-treated films calculated by eq 3 is 0.5 cm^2 $V^{-1}s^{-1}$, which significantly surpasses that of the untreated film of 0.25 cm^2 V^{-1} s^{-1}. The enhanced performance can be attributed to grain growth and a reduction in defect-related nonradiative recombination pathways after NH_3 plasma processing. In fact, the role of NH_3 plasma in $CsPbBr_3$ film deposition is analogous to that of the NH_2 and NH functional groups in solution-based processes. During film deposition, the NH_3 plasma generates active species such as hydrogen (H), amine (NH), and amino (NH_2) groups.[39] As shown in Figure S6, the concentrations of H, NH, and NH_2 groups increase with increasing the NH_3 flow rate. The nitrogen atoms in NH_2 or NH groups possess lone pairs of electrons to function as Lewis bases. As displayed in Figure S7, it is suggested that during film deposition these species can coordinate with undercoordinated Pb^{2+} ions, which act as Lewis acids. This temporary coordination modifies the local chemical environment of Pb^{2+}, reducing its reactivity and effectively "passivating" the ions. As a result, uncontrolled nucleation is suppressed, slowing the crystallization process and facilitating the formation of larger, more well-defined grains with fewer grain boundaries. As the concentration of NH and NH_2 groups increases, the excessive crystallization of Pb^{2+} is more efficiently suppressed, and the growth of larger $CsPbBr_3$ grains is promoted. In addition, the NH_3 plasma treatment passivates

https://doi.org/10.1021/acsaelm.5c00374
ACS Appl. Electron. Mater. 2025, 7, 5404−5411

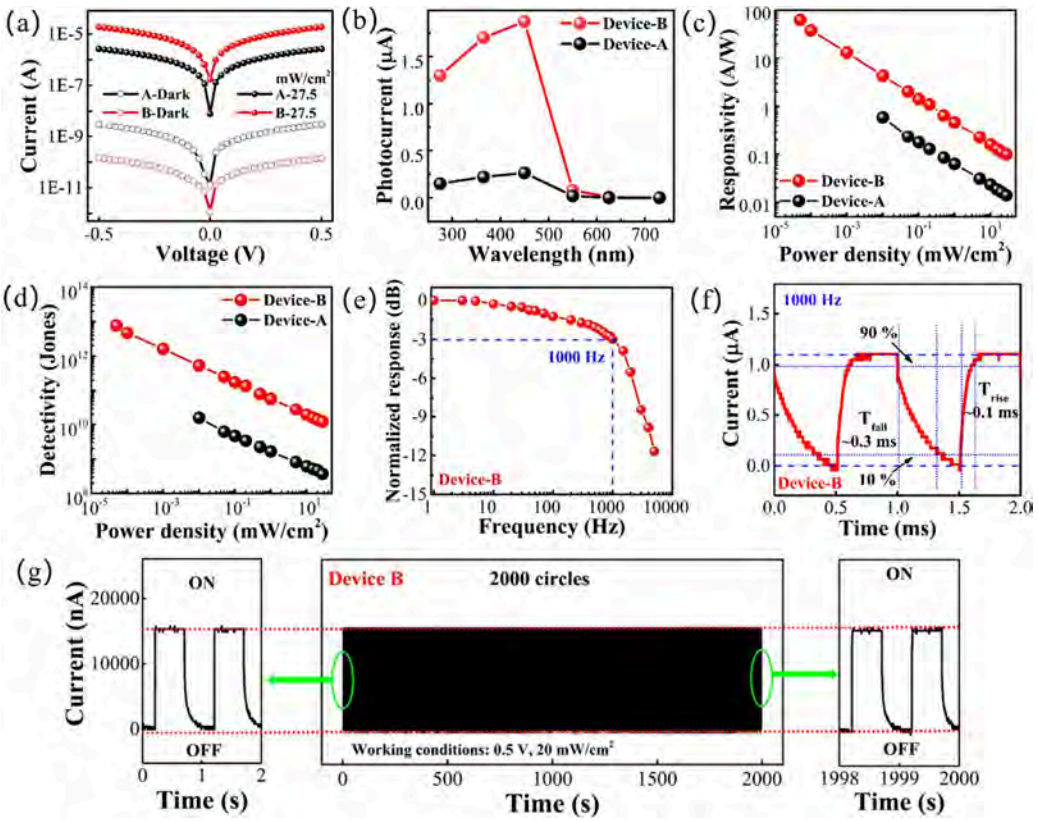

Figure 5. (a) Logarithmic $I-V$ curves of the photodetectors composed of $CsPbBr_3$ films prepared without NH_3 plasma (device A) and with NH_3 plasma at a flow rate of 15 sccm (device B), measured in darkness and under 450 nm illumination with a power density of 27.5 mW cm^{-2}. The effective area of the photodetectors is approximately 0.68 mm^2, where an interdigital Au electrode with a 50 μm spacing is deposited by magnetron sputtering using a mask. (b) Photocurrents of devices A and B at different wavelengths using a bias voltage of 0.5 V and light power density of 27.5 mW cm^{-2}. Dependence of (c) responsivity (R) and (d) specific detectivity (D^*) of devices A and B on illumination power density. (e) Normalized photoresponse of device B versus input signal frequency. (f) Time−response curves, including the rise and decay times of device B, upon illumination with 450 nm light with a power density of 20 mW cm^{-2} at a bias voltage of 0.5 V. The rise time and decay time are defined as the durations required for the photocurrent to increase from 10% to 90% and decrease from 90% to 10% of its steady-state value, respectively, during light switching.[43] (g) Current−time ($I-t$) curves of device B at a bias voltage of 0.5 V upon irradiation with a 20 mW cm^{-2} laser.

defects at the film surface and grain boundaries to improve the overall surface morphology and reduce the number of defect states. The combined effects enhance the film quality by improving the grain size and uniformity.

To evaluate the potential of $CsPbBr_3$ films in optoelectronic applications, planar metal−semiconductor−metal (MSM) photodetectors are fabricated. Figure 5a and Figure S8 show the $I-V$ characteristics of devices A and B, measured in darkness and under illumination by a 450 nm laser with different power densities. At a bias voltage of 0.5 V, the dark current (I_d) of device B is significantly smaller (0.14 nA) than that of device A (3.11 nA). However, under illumination with a power of 27.5 mW cm^{-2}, the photocurrent (I_p) of device B reaches 18.7 μA, which is higher than that of device A of 2.6 μA. This leads to a significant increase in the ON/OFF current ratio of the photodetector, from approximately 6.0×10^2 (device A) to $\sim 1.0 \times 10^5$ (device B), under 450 nm illumination at a power density of 27.5 mW cm^{-2} and a bias voltage of 0.5 V. Figure 5b further demonstrates that device B consistently outperforms device A across a range of excitation wavelengths, highlighted by a significant improvement in the ON/OFF current ratio. The enhanced performance is attributed to the larger grain size and reduced defect density in the $CsPbBr_3$ film of device B. They also contribute to a wider linear dynamic range (LDR), calculated using the formula $LDR = 20 \cdot \log(P_{max}/P_{min})$,[40] compared to device A (Figure S9). The responsivity as a function of incident light power under different light illuminations is presented in Figure 5c and Figure S10a. The responsivity of the photodetectors is quantified by the formula $R = (I_p - I_d)/(P \cdot S)$, where P is the incident light intensity and S is the effective irradiated area.[41] As shown in Figure 5c, the responsivity R of device B exhibits a response of 62.7 A/W, which is more than 100 times higher than that of device A of 0.6 A/W. Figure 5d and Figure S10b show the relationship between D^* and the incident irradiance power under various light illuminations. As shown in Figure 5d, the specific detectivity (D^*) of device B, calculated by the formula of $D^* = R \cdot S^{1/2}/(2e \cdot I_{dark})^{1/2}$,[42] reaches 7.7×10^{12} Jones, which surpasses 1.6×10^{10} Jones of device A.

To investigate the dynamic photoresponse, the current−time ($I-t$) curves of the devices are acquired under 450 nm light illumination at 20 mW and a bias of 0.5 V (Figure 5g and Figure S11). After 2000 s (2000 cycles) of operation, the current of device A increases (Figure S11), while that of device B remains stable (Figure 5g), indicating that device B has more reliable and reversible optical switching characteristics. The −3 dB cutoff frequency (f-3 dB) of device B is determined to be approximately 1000 Hz (Figure 5e), compared to 100 Hz for device A (Figure S12), highlighting the superior high-frequency stability of device B. Furthermore, the response

https://doi.org/10.1021/acsaelm.5c00374
ACS Appl. Electron. Mater. 2025, 7, 5404−5411

and decay times of device B at 1000 Hz are 0.1 and 0.3 ms (Figure 5f), respectively, which are significantly faster than those of device A (0.5 and 3.2 ms, respectively; Figure S13). In other words, the photodetector with the plasma-processed $CsPbBr_3$ film has significantly better characteristics such as a responsivity of 62.7 A/W, a detectivity of 7.7×10^{12} Jones, an ultrafast response time of 0.1/0.3 ms, and exceptional stability, all of which are better than those of the device composed of the untreated $CsPbBr_3$ film, which shows a responsivity of 0.6 A/W, a detectivity of 1.6×10^{10} Jones, and a response time of 0.5/3.2 ms. Table S2 (Supporting Information) compares the performance of recently reported lead halide perovskite photodetectors to similar MSM architectures. Notably, our device, based on $CsPbBr_3$ films fabricated using NH_3 plasma, demonstrates superior responsivity, rapid response, and high detectivity. These results highlight the effectiveness of NH_3 plasma-assisted growth in advancing the performance of $CsPbBr_3$ perovskite photodetectors.

4. CONCLUSIONS

The significant advantages of NH_3 plasma processing in improving the quality and performance of $CsPbBr_3$ perovskite films are demonstrated. The NH_3 plasma promotes grain growth, reduces grain boundaries, and eliminates defect states, resulting in a notable reduction in the defect density from 7.9×10^{12} cm^{-3} to 6.8×10^{12} cm^{-3}. As a result, the photodetector fabricated with the plasma-treated film has exceptional characteristics such as high responsivity, detectivity, ultrafast response times, and stability, all of which substantially outperform the device without plasma processing. The enhanced performance and stability of NH_3 plasma-treated $CsPbBr_3$ films make them highly promising candidates for applications in optical communications and environmental sensing.

■ ASSOCIATED CONTENT

Supporting Information

The Supporting Information is available free of charge at https://pubs.acs.org/doi/10.1021/acsaelm.5c00374.

XRD, Raman, and optical absorption spectra of $CsPbBr_3$ films prepared by CVD; photocurrents, *I*−V characteristics, and time−response curves of the Pb-based perovskite photodetectors (PDF)

■ AUTHOR INFORMATION

Corresponding Authors

Rui Huang − *School of Physics and Electronic Engineering, Hanshan Normal University, Chaozhou 521041, China;* orcid.org/0000-0002-3204-5663; Email: rhuang@hstc.edu.cn

Paul K. Chu − *Department of Physics, Department of Materials Science and Engineering, and Department of Biomedical Engineering, City University of Hong Kong, Hong Kong, China;* orcid.org/0000-0002-5581-4883; Email: paul.chu@cityu.edu.hk

Authors

Zewen Lin − *School of Physics and Electronic Engineering, Hanshan Normal University, Chaozhou 521041, China*

Zhenxu Lin − *School of Physics and Electronic Engineering, Hanshan Normal University, Chaozhou 521041, China;* orcid.org/0000-0002-6758-6443

Jie Song − *School of Physics and Electronic Engineering, Hanshan Normal University, Chaozhou 521041, China*

Haixia Wu − *School of Physics and Electronic Engineering, Hanshan Normal University, Chaozhou 521041, China*

Kaitao Chen − *School of Physics and Electronic Engineering, Hanshan Normal University, Chaozhou 521041, China*

Li Xia − *School of Physics and Electronic Engineering, Hanshan Normal University, Chaozhou 521041, China*

Yi Zhang − *School of Physics and Electronic Engineering, Hanshan Normal University, Chaozhou 521041, China*

Hongliang Li − *School of Physics and Electronic Engineering, Hanshan Normal University, Chaozhou 521041, China*

Yanqing Guo − *School of Physics and Electronic Engineering, Hanshan Normal University, Chaozhou 521041, China*

Huihong Lin − *School of Physics and Electronic Engineering, Hanshan Normal University, Chaozhou 521041, China;* orcid.org/0000-0002-1635-2786

Complete contact information is available at: https://pubs.acs.org/10.1021/acsaelm.5c00374

Author Contributions

Zewen Lin, Zhenxu Lin, and Jie Song contributed equally to this work. Zewen Lin: investigation, data curation, formal analysis, writing − original draft; Zhenxu Lin: investigation, data curation, formal analysis, writing − original draft; Jie Song: investigation, data curation, formal analysis, writing − original draft; Haixia Wu: formal analysis; Kaitao Chen: investigation; Li Xia: formal analysis; Yi Zhang: investigation; Hongliang Li: formal analysis; Yanqing Guo: formal analysis; Huihong Lin: formal analysis; Paul K. Chu: supervision, funding acquisition, writing − review and editing; Rui Huang: formal analysis, project administration, funding acquisition, resources, supervision, writing − review and editing.

Notes

The authors declare no competing financial interest.

■ ACKNOWLEDGMENTS

The authors would like to acknowledge the support of the Guangdong Basic and Applied Basic Research Foundation, Research Projects of the Department of Education of Guangdong Province (2021ZDJS039, 2024ZDZX1026), Guangdong Basic and Applied Basic Research Foundation (2024A1515012339), City University of Hong Kong Donation Research Grants (9220061 and DON-RMG 9229021), Program of Hanshan Normal University (XTP202402), and College Students' Innovation and Entrepreneurship Training Program (202110578008 and S202310578021).

■ REFERENCES

(1) Elkhouly, K.; Goldberg, I.; Zhang, X.; Annavarapu, N.; Hamdad, S.; Croes, G.; Rolin, C.; Genoe, J.; Qiu, W.; Gehlhaar, R.; Heremans, P. Electrically Assisted Amplified Spontaneous Emission in Perovskite Light-Emitting Diodes. *Nat. Photonics* **2024**, *18* (2), 132−138.

(2) Liu, Y.; Stasio, F. D.; Bi, C.; Zhang, J.; Xia, Z.; Shi, Z.; Manna, L. Near-Infrared Light Emitting Metal Halides: Materials, Mechanisms, and Applications. *Adv. Mater.* **2024**, *36* (21), No. 2312482.

(3) Zhang, Q.; Zheng, W.; Wan, Q.; Liu, M.; Feng, X.; Kong, L.; Li, L. Confined Synthesis of Stable and Uniform $CsPbBr_3$ Nanocrystals with High Quantum Yield up to 90% by High Temperature Solid-State Reaction. *Adv. Opt. Mater.* **2021**, *9* (11), No. 2002130.

(4) Zhong, Y.; Liao, K.; Du, W.; Zhu, J.; Shang, Q.; Zhou, F.; Wu, X.; Sui, X.; Shi, J.; Yue, S.; Wang, Q.; Zhang, Y.; Zhang, Q.; Hu, X.; Liu, X. Large-Scale Thin $CsPbBr_3$ Single-Crystal Film Grown on

Sapphire via Chemical Vapor Deposition: Toward Laser Array Application. *ACS Nano* **2020**, *14* (11), 15605−15615.
(5) Han, Z.; Fu, W.; Zou, Y.; Gu, Y.; Liu, J.; Huang, B.; Yu, D.; Cao, F.; Li, X.; Xu, X.; Zeng, H. Oriented Perovskite Growth Regulation Enables Sensitive Broadband Detection and Imaging of Polarized Photons Covering 300−1050 nm. *Adv. Mater.* **2021**, *33* (11), No. 2003852.
(6) Cong, H.; Chu, X.; Wan, F.; Chu, Z.; Wang, X.; Ma, Y.; Jiang, J.; Shen, L.; You, J.; Xue, C. Broadband Photodetector Based on Inorganic Perovskite $CsPbBr_3$/GeSn Heterojunction. *Small Methods* **2021**, *5* (8), No. 2100517.
(7) Dong, Q.; Chen, M.; Liu, Y.; Eickemeyer, F. T.; Zhao, W.; Dai, Z.; Yin, Y.; Jiang, C.; Feng, J.; Jin, S.; Liu, S.; Zakeeruddin, S. M.; Gratzel, M.; Padture, N. P.; Shi, Y. Flexible Perovskite Solar Cells with Simultaneously Improved Efficiency, Operational Stability, and Mechanical Reliability. *Joule* **2021**, *5* (6), 1587.
(8) Kim, J. S.; Heo, J.-M.; Park, G.-S.; Woo, S.-J.; Cho, C.; Yun, H. J.; Kim, D.-H.; Park, J.; Lee, S.-C.; Park, S.-H.; Yoon, E.; Greenham, N. C.; Lee, T.-W. Ultra-Bright, Efficient and Stable Perovskite Light-Emitting Diodes. *Nature* **2022**, *611* (7937), 688−694.
(9) Park, S. M.; Wei, M. Y.; Xu, J.; Atapattu, H. R.; Eickemeyer, F. T.; Darabi, K.; Grater, L.; Yang, Y.; Liu, C.; Teale, S.; Chen, B.; Chen, H.; Wang, T. H.; Zeng, L.; Maxwell, A.; Wang, Z. W.; Rao, K. R.; Cai, Z. Y.; Zakeeruddin, S. M.; Pham, J. T.; Risko, C. M.; Amassian, A.; Kanatzidis, M. G.; Graham, K. R.; Grätzel, M.; Sargent, E. H. Engineering Ligand Reactivity Enables High-Temperature Operation of Stable Perovskite Solar Cells. *Science* **2023**, *381* (6654), 209−215.
(10) Cao, Y.; Zhang, X.; Zhao, K.; Wei, Y.; Zhang, L.; Zhang, H.; Wang, W.; Cui, C.; Wang, P.; Lin, P.; Wu, X.; Song, C.; Ni, Z.; Xue, J.; Wang, R.; Xu, L. In situ Crosslinked Robust Molecular Zipper at the Buried Interface for Perovskite Photovoltaics. *Adv. Funct. Mater.* **2025**, *35*, No. 2422205.
(11) Tong, G.; Li, H.; Li, D.; Zhu, Z.; Xu, E.; Li, G.; Yu, L.; Xu, J.; Jiang, Y. Dual-Phase $CsPbBr_3$−$CsPb_2Br_5$ Perovskite Thin Films via Vapor Deposition for High-Performance Rigid and Flexible Photodetectors. *Small* **2018**, *14* (7), No. 1702523.
(12) Lou, S.; Huang, L.; Liu, B.; Si, S.; Xuan, T.; Lan, B.; Zhang, J.; Li, M.; Wang, J. In Situ Growth of $CsPbBr_3$ Perovskite Nanocrystals in Lead-Based Matrix toward Significantly Enhanced Water/Photo Stabilities. *Adv. Opt. Mater.* **2022**, *10* (1), No. 2101448.
(13) Kang, C. H.; Dursun, I.; Liu, G.; Sinatra, L.; Sun, X.; Kong, M.; Pan, J.; Maity, P.; Ooi, E.-N.; Ng, T. K.; Mohammed, O. F.; Bakr, O. M.; Ooi, B. S. High-Speed Colour-Converting Photodetector with All-Inorganic $CsPbBr_3$ Perovskite Nanocrystals for Ultraviolet Light Communication. *Light Sci. Appl.* **2019**, *8* (1), 94.
(14) Yang, Z.; Xu, Q.; Wang, X.; Lu, J.; Wang, H.; Li, F.; Zhang, L.; Hu, G.; Pan, C. Large and Ultrastable All-Inorganic $CsPbBr_3$ Monocrystalline Films: Low-Temperature Growth and Application for High-Performance Photodetectors. *Adv. Mater.* **2018**, *30* (44), No. 1802110.
(15) Zhang, J.; Pan, X.; Sun, J.; Zhou, H.; Zhang, G.; Ding, L. A-Site Cation Exchange Enables a High-Performance $CsPbBr_3$ Photodetector for Laser Eavesdropping Systems. *Adv. Opt. Mater.* **2024**, *12* (5), No. 2301848.
(16) Liu, Z.; Peters, J. A.; Bayikadi, K. S.; Klepov, V.; Pan, L.; Pandey, I. R.; Kanatzidis, M. G.; Wessels, B. W. Defects of Perovskite Semiconductor $CsPbBr_3$ Investigated via Photoluminescence and Thermally Stimulated Current Spectroscopies. *J. Appl. Phys.* **2023**, *134* (24), No. 245101.
(17) Grandhi, G. K.; Hardy, D.; Krishnaiah, M.; Vargas, B.; Al-Anesi, B.; Suryawanshi, M. P.; Solis-Ibarra, D.; Gao, F.; Hoye, R. L. Z.; Vivo, P. Wide-Bandgap Perovskite-Inspired Materials: Defect-Driven Challenges for High-Performance Optoelectronics. *Adv. Funct. Mater.* **2024**, *34* (50), No. 2307441.
(18) Zhu, J.; He, B.; Gong, Z.; Ding, Y.; Zhang, W.; Li, X.; Zong, Z.; Chen, H.; Tang, Q. Grain Enlargement and Defect Passivation with Melamine Additives for High Efficiency and Stable $CsPbBr_3$ Perovskite Solar Cells. *ChemSusChem* **2020**, *13* (7), 1834−1843.
(19) Kim, J.-H.; Kang, D.-H.; Lee, D.-N.; Park, N.-G. Effect of Functional Groups in Passivating Materials on Stability and Performance of Perovskite Solar Cells. *J. Mater. Chem. A* **2023**, *11* (27), 15014−15021.
(20) Jiang, X.; Yang, G.; Zhang, B.; Wang, L.; Yin, Y.; Zhang, F.; Yu, S.; Liu, S.; Bu, H.; Zhou, Z.; Sun, L.; Pang, S.; Guo, X. Understanding the Role of Fluorine Groups in Passivating Defects for Perovskite Solar Cells. *Angew. Chem.* **2023**, *135* (45), No. e202313133.
(21) He, Q.; Pan, S.; Zhang, T.; Chen, X.; Chen, A.; Xu, G.; Zhou, K.; Li, J.; Zhu, H.; Bakr, O. M.; Pan, J. Boosting Photovoltaic Efficiency: The Role of Functional Group Distribution in Perovskite Film Passivation. *Small* **2025**, *21* (5), No. 2410481.
(22) Feng, W.; Tan, Y.; Yang, M.; Jiang, Y.; Lei, B.-X.; Wang, L.-Z.; Wu, W.-Q. Small Amines Bring Big Benefits to Perovskite-Based Solar Cells and Light-Emitting Diodes. *Chem.* **2022**, *8* (2), 351−383.
(23) Liu, B.; Chen, H.; Cao, J.; Chen, X.; Xie, J.; Shu, Y.; Yan, F.; Huang, W.; Qin, T. Imidazole Derivative Assisted Crystallization for High-Efficiency Mixed Sn−Pb Perovskite Solar Cells. *Adv. Funct. Mater.* **2024**, *34* (6), No. 2310828.
(24) Luo, M.; Wei, C.; Wu, Y.; Lei, W.; Zhang, X.; Zeng, H. All-Inorganic Perovskite Film Photodetectors with Tailored Deposition Techniques and Component Engineering. *J. Mater. Chem. C* **2024**, *12* (31), 11675−11711.
(25) Calisi, N.; Galvanetto, E.; Borgioli, F.; Martinuzzi, S. M.; Bacci, T.; Caporali, S. Thin Films Deposition of Fully Inorganic Metal Halide Perovskites: A Review. *Mater. Sci. Semicond. Process.* **2022**, *147*, No. 106721.
(26) Covella, S.; Armenise, V.; Rehman, M. O. U.; Aktas, E.; Fracassi, F.; Palumbo, F.; Colella, S.; Abate, A.; Listorti, A. Plasma-Based Modification of Tin Halide Perovskite Interfaces for Photovoltaic Applications. *ACS Appl. Mater. Interfaces* **2024**, *16* (37), 49392.
(27) Perrotta, A.; Covella, S.; Russo, F.; Palumbo, F.; Milella, A.; Armenise, V.; Fracassi, F.; Rizzo, A.; Colella, S.; Kaiser, W.; Alothman, A. A.; Mosconi, E.; De Angelis, F.; Listorti, A. Plasma-Driven Atomic-Scale Tuning of Metal Halide Perovskite Surfaces: Rationale and Photovoltaic Application. *Sol. RRL* **2023**, *7* (18), No. 2300345.
(28) Ma, X.; Zheng, H.; Wang, Y.; Liu, Y.; Liu, Q.; Xiao, J.; Pang, S.; Dong, Z.; Zhang, Y.; Yan, K.; Zou, D.; Hu, J.; Hou, S. Plasma Sputtering Halide Perovskite for Photovoltaic Applications. *ACS Mater. Lett.* **2024**, *6* (11), 5076.
(29) Guo, R.; Wang, X.; Jia, X.; Guo, X.; Li, J.; Li, Z.; Sun, K.; Jiang, X.; Alvianto, E.; Shi, Z.; Schwartzkopf, M.; Muller-Buschbaum, P.; Hou, Y. Refining the Substrate Surface Morphology for Achieving Efficient Inverted Perovskite Solar Cells. *Adv. Energy Mater.* **2023**, *13* (43), No. 2302280.
(30) Casanova-Chafer, J.; Garcia-Aboal, R.; Liobet, E.; Atienzar, P. Enhanced CO_2 Sensing by Oxygen Plasma-Treated Perovskite−Graphene Nanocomposites. *ACS Sens.* **2024**, *9* (2), 830−839.
(31) Peng, C.; Qian, B.; Yin, Q.; Xu, M.; Jin, Y.; Wang, C.; Ma, X.; Xu, T. Surface passivation of the methylammonium lead iodide ($CH_3NH_3PbI_3$) by oxygen plasma to improve solar cell efficiency. *Vacuum* **2023**, *207*, No. 111675.
(32) Huang, Q.; Fu, C.; Shen, Y.; Wang, H.; Wu, Z.; Liang, Z.; Tian, C.; Wu, D.; Qi, F.; Pu, Y.; Zhang, N.; Wang, M.; Tang, X. Boosting CO_2 Conversion by Synergy of Lead-Free Perovskite Cs_2SnCl_6 and Plasma with H_2O. *J. Phys. Chem. Lett.* **2023**, *14* (40), 8922−8929.
(33) Han, D.; Yang, K.; Bai, C.; Chen, F.; Sun, Z.; Wang, Y.; Ji, H.; Yang, Z.; Tang, X. Thermal and Chemical Durability of Metal Halide Perovskite $CsPbBr_3$ Single Crystals. *Chem. Eng. J.* **2023**, *475*, No. 146209.
(34) Lin, Z.; Huang, R.; Li, S.; Liu, S.; Song, J.; Panmai, M.; Lan, S. Ultralow Threshold Lasing from a Continuous-Wave-Pumped SiN_x/$CsPbBr_3$/Ag Thin Film Mediated by the Whispering Gallery Modes of a SiO_2 Microsphere. *J. Phys. Chem. Lett.* **2022**, *13* (42), 9967−9974.
(35) Lin, Z.; Li, H.; Huang, R.; Zhang, Y.; Song, J.; Li, H.; Guo, Y.; Song, C.; Robertson, J. Defect Emission and Optical Gain in SiC_xO_y:H Films. *ACS Appl. Mater. Interfaces* **2017**, *9* (27), 22725.
(36) Lin, K. H.; Liou, S. C.; Chen, W. L.; Wu, C. L.; Lin, G. R.; Chang, Y. M. Tunable and Stable UV-NIR Photoluminescence from

https://doi.org/10.1021/acsaelm.5c00374
ACS Appl. Electron. Mater. 2025, 7, 5404−5411

Annealed SiO_x with Si Nanoparticles. *Opt. Express* **2013**, *21* (20), 23416−23424.
(37) Demkiv, T. M.; Myagkota, S. V.; Malyi, T.; Pushak, A. S.; Vistovskyy, V. V.; Yakibchuk, P. M.; Shapoval, O. V.; Mitina, N. E.; Zaichenko, A. S.; Voloshinovskii, A. S. Luminescence Properties of $CsPbBr_3$ Nanocrystals Dispersed in a Polymer Matrix. *J. Lumin.* **2018**, *198*, 103−107.
(38) Zuleeg, R.; Knoll, P. Space-Charge-Limited Currents in Heteroepitaxial Films of Silicon Grown on Sapphire. *Appl. Phys. Lett.* **1967**, *11* (6), 183−185.
(39) Lin, Z.; Huang, R.; Zhang, W.; Zhang, Y.; Song, J.; Li, H.; Hou, D.; Guo, Y.; Song, C.; Wan, N.; Chu, P. K. Highly Luminescent and Stable Si-Based $CsPbBr_3$ Quantum Dot Thin Films Prepared by Glow Discharge Plasma with Real-Time and In Situ Diagnosis. *Adv. Funct. Mater.* **2018**, *28* (50), No. 1805214.
(40) Chen, J.; Hou, L.; Rao, T.; Wang, W.; Chang, B.; Yuan, Y.; Wu, X.; Lin, P.; Wang, P.; Cui, C.; Ni, Z.; Xu, L. Regulating cation arrangements for high-performance lead-free $Cs_2AgBiBr_6$ double perovskite photodetectors via modified green antisolvent engineering. *J. Mater. Sci. Technol.* **2025**, *232*, 115−122.
(41) Krishnaiah, M.; Kim, S.; Kumar, A.; Mishra, D.; Seo, S. G.; Jin, S. H. Physically Detachable and Operationally Stable Cs_2SnI_6 Photodetector Arrays Integrated with μ-LEDs for Broadband Flexible Optical Systems. *Adv. Mater.* **2022**, *34* (17), No. 2109673.
(42) Gao, W.; Liu, X.; Jin, H.; Li, W.; Wang, X.; Huang, R.; Xing, G.; Dong, H.; Zhou, Y.; Wu, Z.; Ran, C. Seed-Crystal-Assisted Space-Confined Growth of $FASnI_3$ Quasi-Single-Crystal Thick Films and Their Photodetection Characteristics. *ACS Energy Lett.* **2024**, *9* (10), 5045−5055.
(43) Zheng, Y.; Zhan, Z.; Chen, Q.; Chen, J.; Luo, J.; Cai, J.; Zhou, Y.; Chen, K.; Xie, W. Highly Sensitive Perovskite Photoplethysmography Sensor for Blood Glucose Sensing Using Machine Learning Techniques. *Adv. Sci.* **2024**, *11* (43), No. 2405681.

https://doi.org/10.1021/acsaelm.5c00374
ACS Appl. Electron. Mater. 2025, 7, 5404−5411

Supporting information

High-Performance Ammonia Plasma-Processed $CsPbBr_3$ Perovskite Photodetectors

Zewen Lin[†,a] *Zhenxu Lin*[†,a] *Jie Song*[†,a] *Rui Huang*[*,a] *Haixia Wu,*[a] *Kaitao Chen,*[a] *Li Xia,*[a] *Yi Zhang,*[a] *Hongliang Li,*[a] *Yanqing Guo,*[a] *Huihong Lin,*[a] *and Paul K. Chu*[*,b]

a. School of Physics and Electronic Engineering, Hanshan Normal University, Chaozhou, 521041, China

b. Department of Physics, Department of Materials Science and Engineering, and Department of Biomedical Engineering, City University of Hong Kong, Tat Chee Avenue, Kowloon, Hong Kong, China

AUTHOR INFORMATION

Corresponding Author

R. Huang - School of Physics and Electronic Engineering, Hanshan Normal University, Chaozhou 521041, China, Email : *rhuang@hstc.edu.cn*

P. K. Chu - Department of Physics, Department of Materials Science and Engineering, and Department of Biomedical Engineering, City University of Hong Kong, Tat Chee Avenue, Kowloon, Hong Kong, China, E-mail: *paul.chu@cityu.edu.hk*

Author Contributions

† Z. Lin, Z. Lin, and J. Song contributed equally to this work.

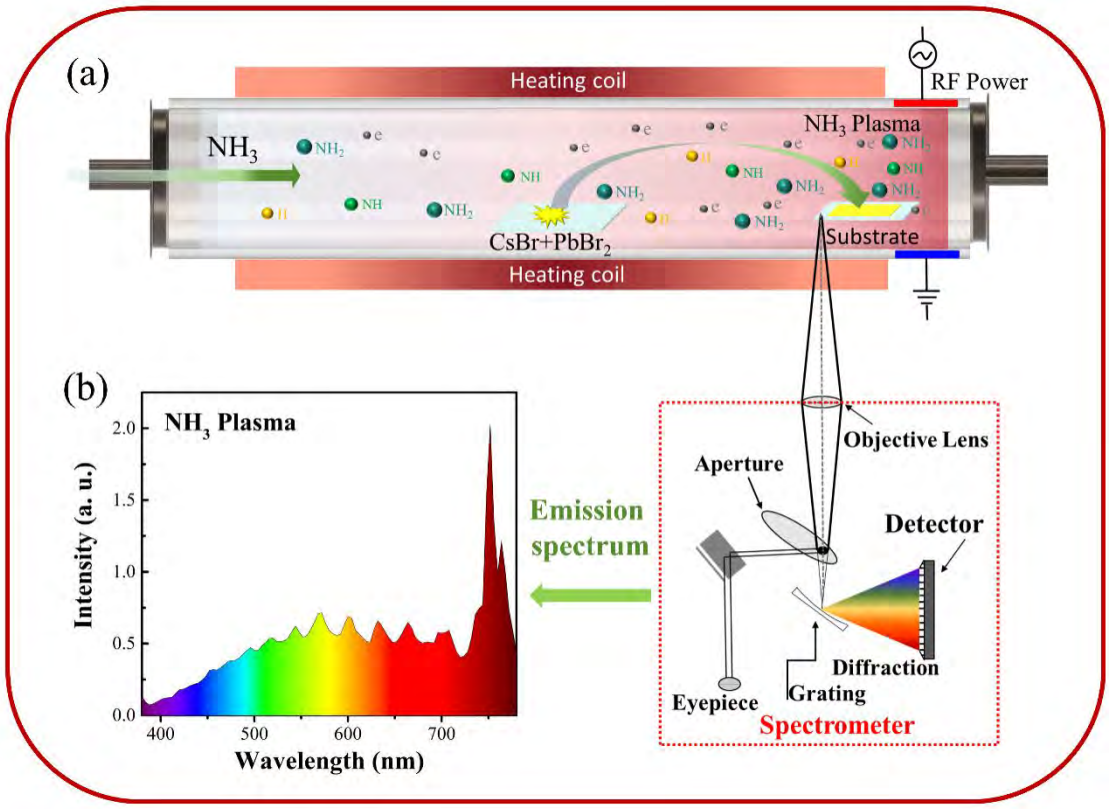

Figure S1. Schematic diagram of the experimental setup and flow. (a) The NH_3 plasma-assisted chemical vapor deposition for synthesizing high-quality $CsPbBr_3$ film; (b) The NH_3 glow discharge plasma diagnostics using optical emission spectroscopy.

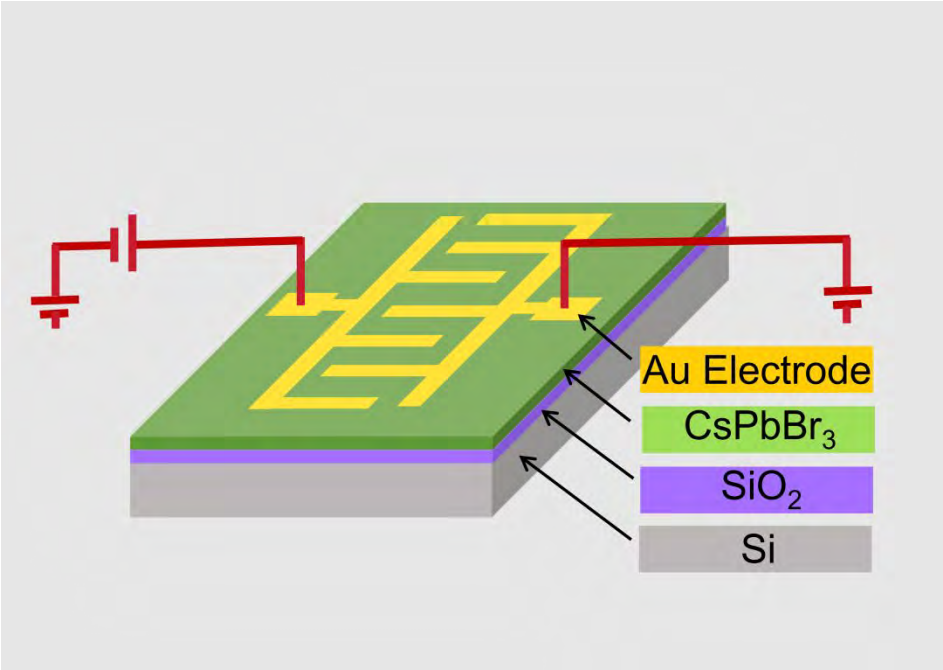

Figure S2. Schematic structure of the photodetector.

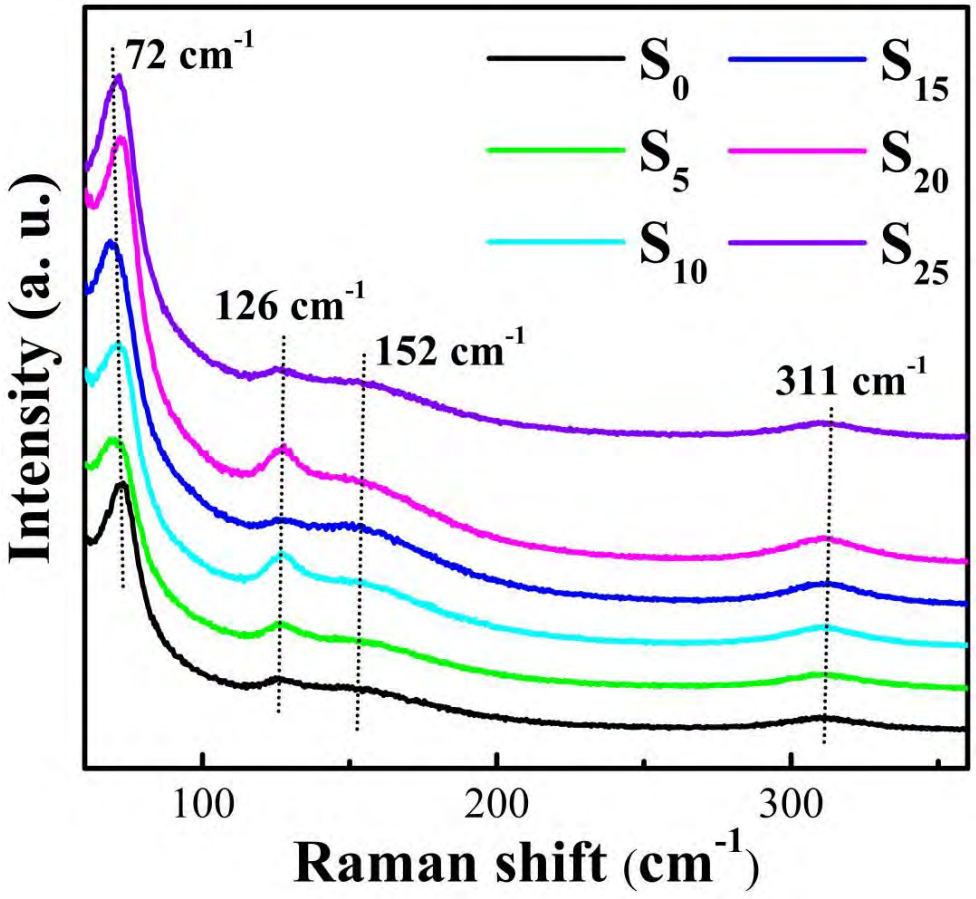

Figure S3. Raman spectra of $CsPbBr_3$ films deposited using different NH_3 flow rates excited by the 633 nm laser.

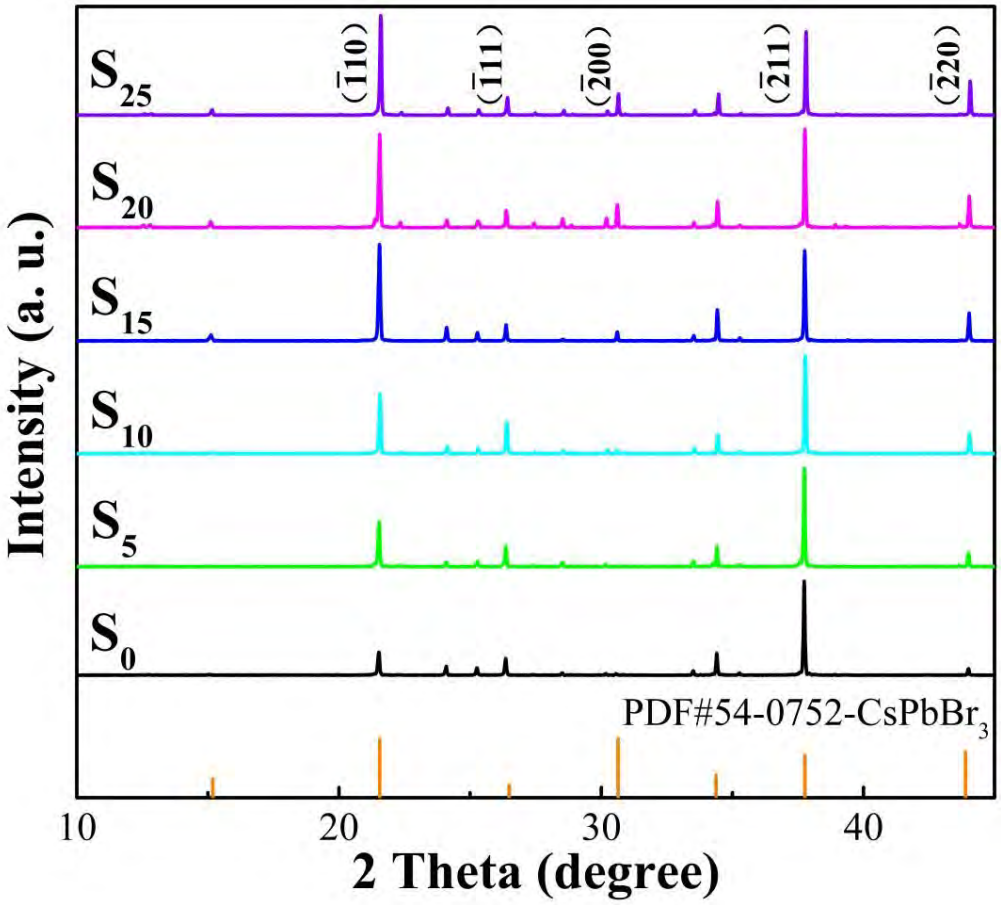

Figure S4. XRD patterns of $CsPbBr_3$ films prepared with different NH_3 flow rates. (S_0) 0 sccm, (S_5) 5 sccm, (S_{10}) 10 sccm, (S_{15}) 15 sccm, (S_{20}) 20 sccm, and (S_{25}) 25 sccm.

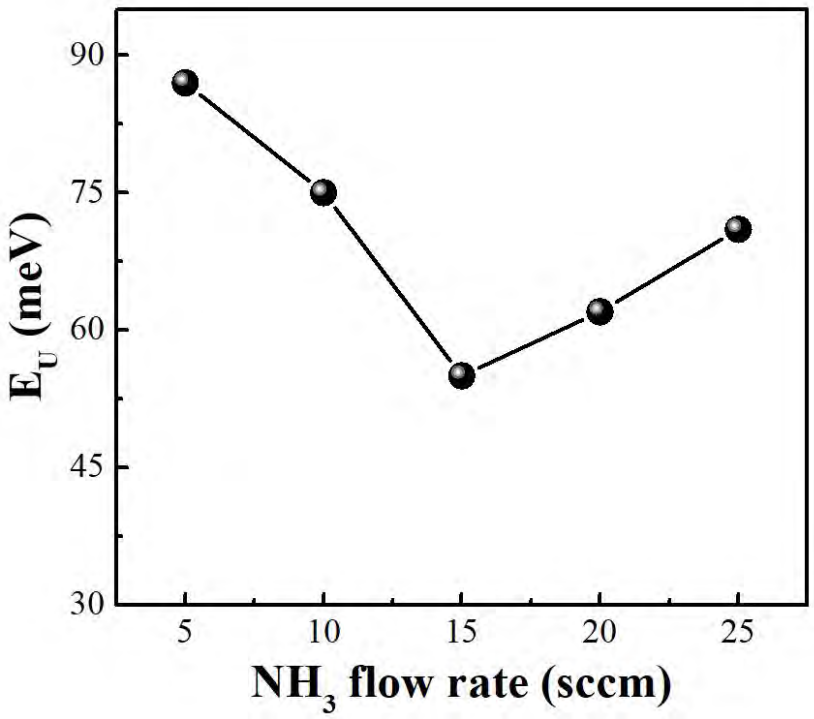

Figure S5. The variation of Urbach energy (E_U) of $CsPbBr_3$ films as a function of NH_3 flow rate. The E_U values were extracted from optical absorption measurements following the method described in Ref. 1-2.

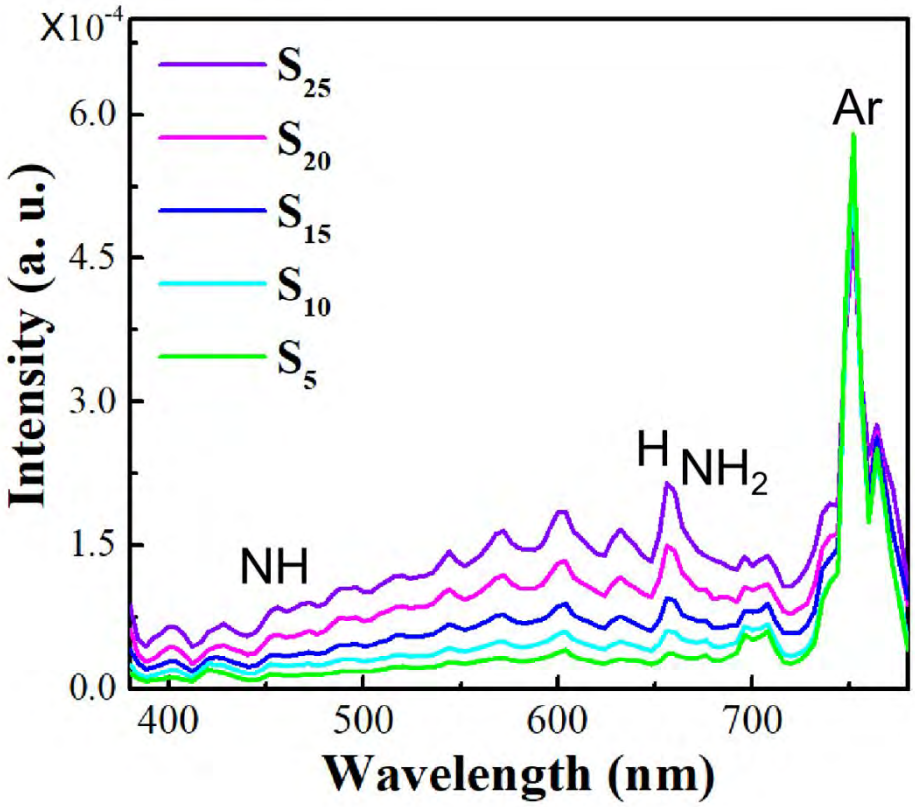

Figure S6. presents the optical emission spectrum of an NH_3+Ar plasma at varying NH_3 flow rates. The spectrum shows a prominent emission band of NH centered around ~450 nm, an intense Ar emission peak near ~750 nm, and a blend of NH_2 emission at ~661 nm overlapping with the H emission band at ~656 nm.

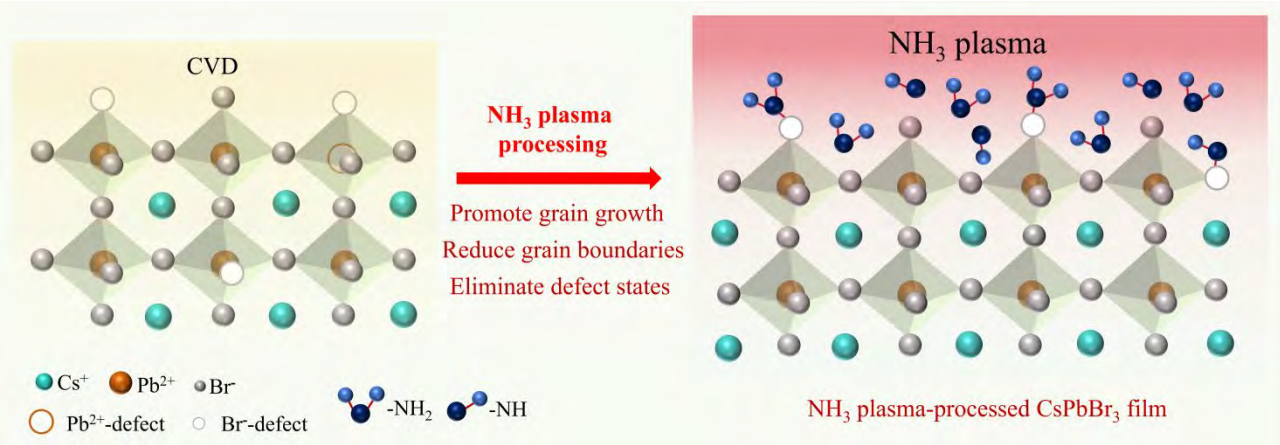

Figure S7. Schematic illustration of NH_3 plasma processing $CsPbBr_3$ films.

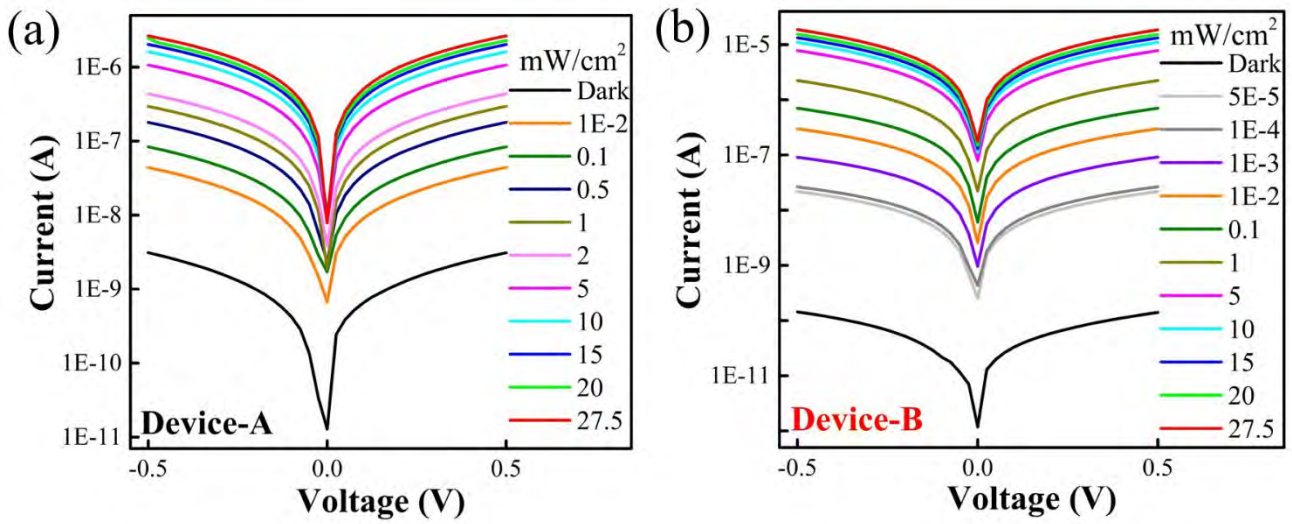

Figure S8. (a) Logarithmic I−V curves of the photodetectors composed of $CsPbBr_3$ films prepared without the NH_3 plasma (device A) and (b) with the NH_3 plasma at a flow rate of 15 sccm (device B), measured in darkness and under 450 nm illumination with different power densities.

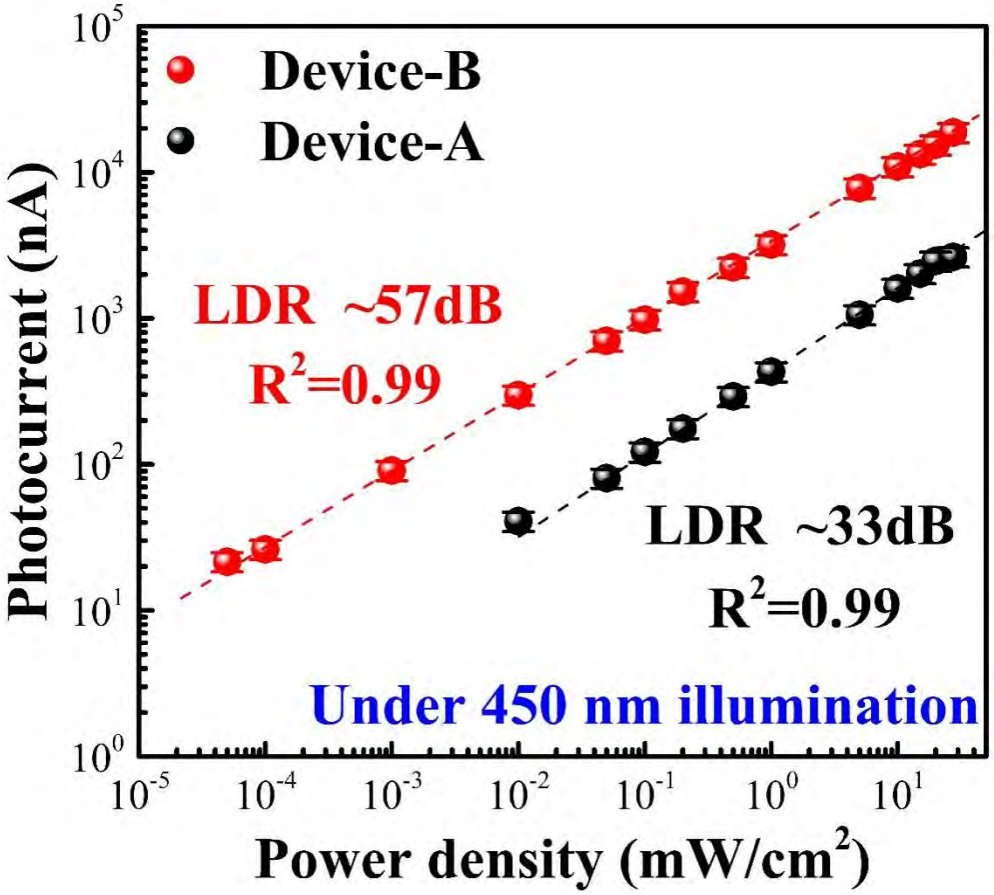

Figure S9. Dependence of photocurrents on illumination power densities for devices A and B at a bias voltage of 0.5 V.

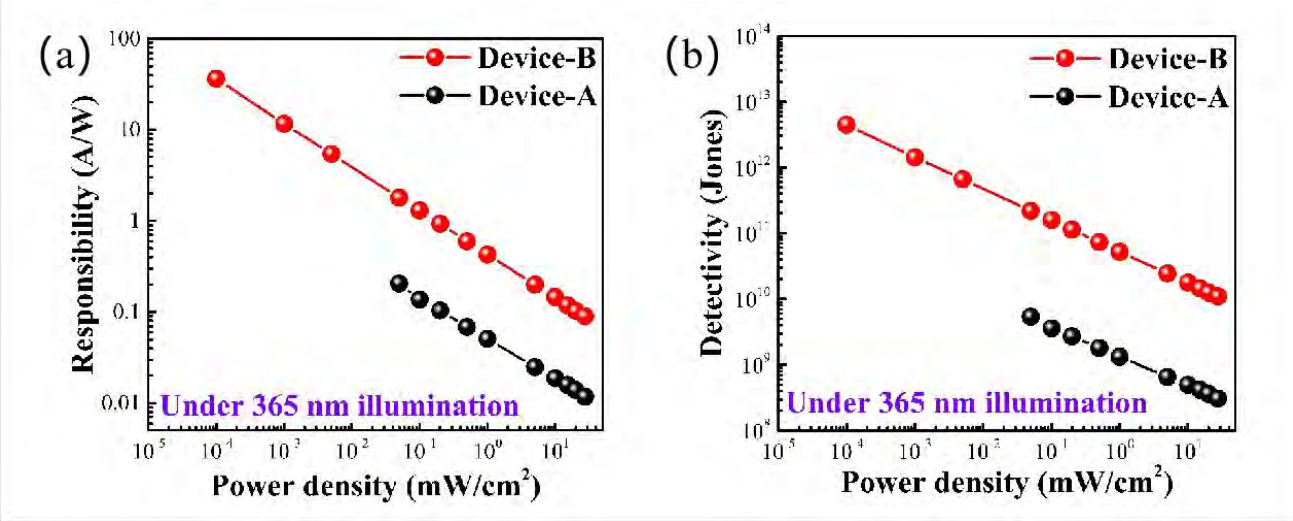

Figure S10. (a) Responsivity (R) and (b) Specific detectivity (D*) of different devices (A and B) under illumination with a 365 nm laser with different illumination power densities.

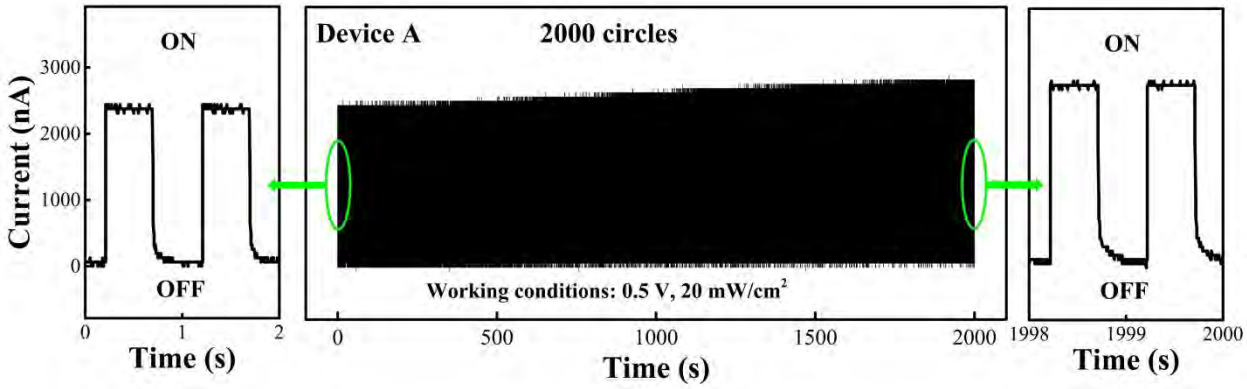

Figure S11. Current-time (I−t) curves of device A at a bias voltage of 0.5 V upon 20 mW cm^{-2} laser illumination.

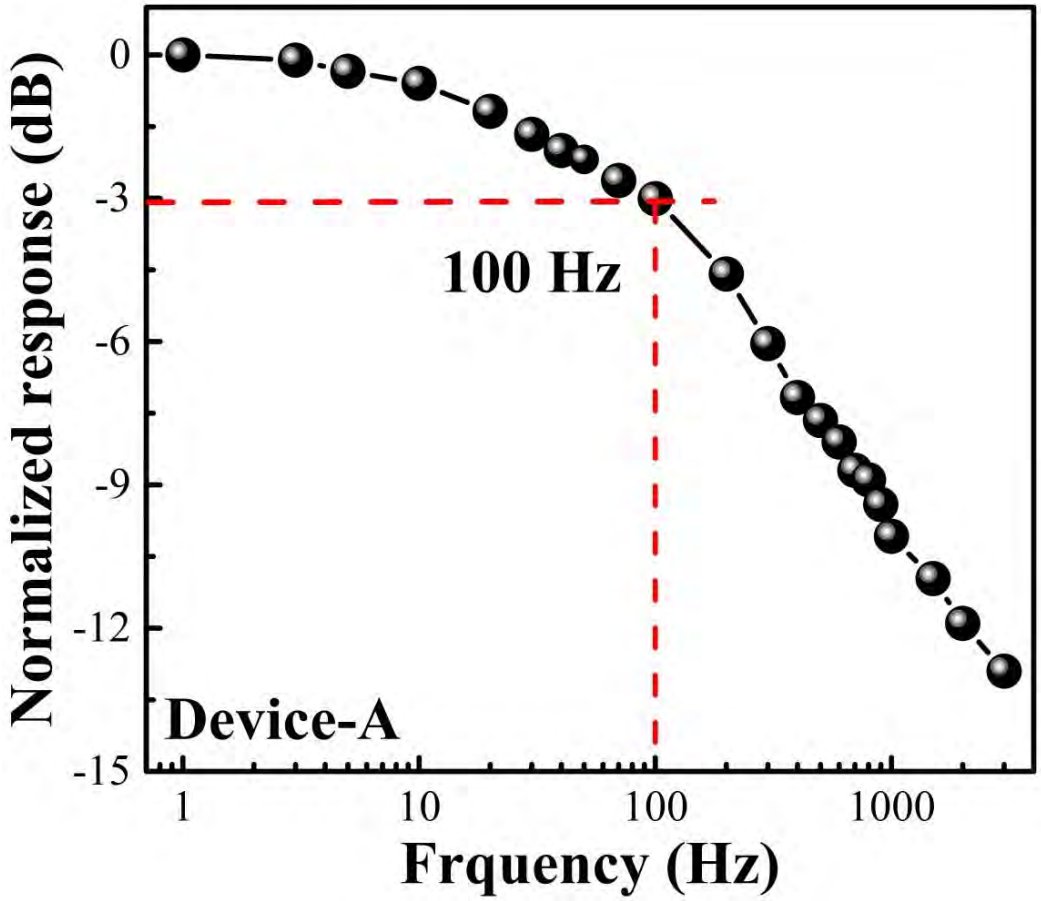

Figure S12. Time-response curve of device A upon 450 nm laser illumination using a power density of 20 mW cm^{-2} and bias of 0.5 V.

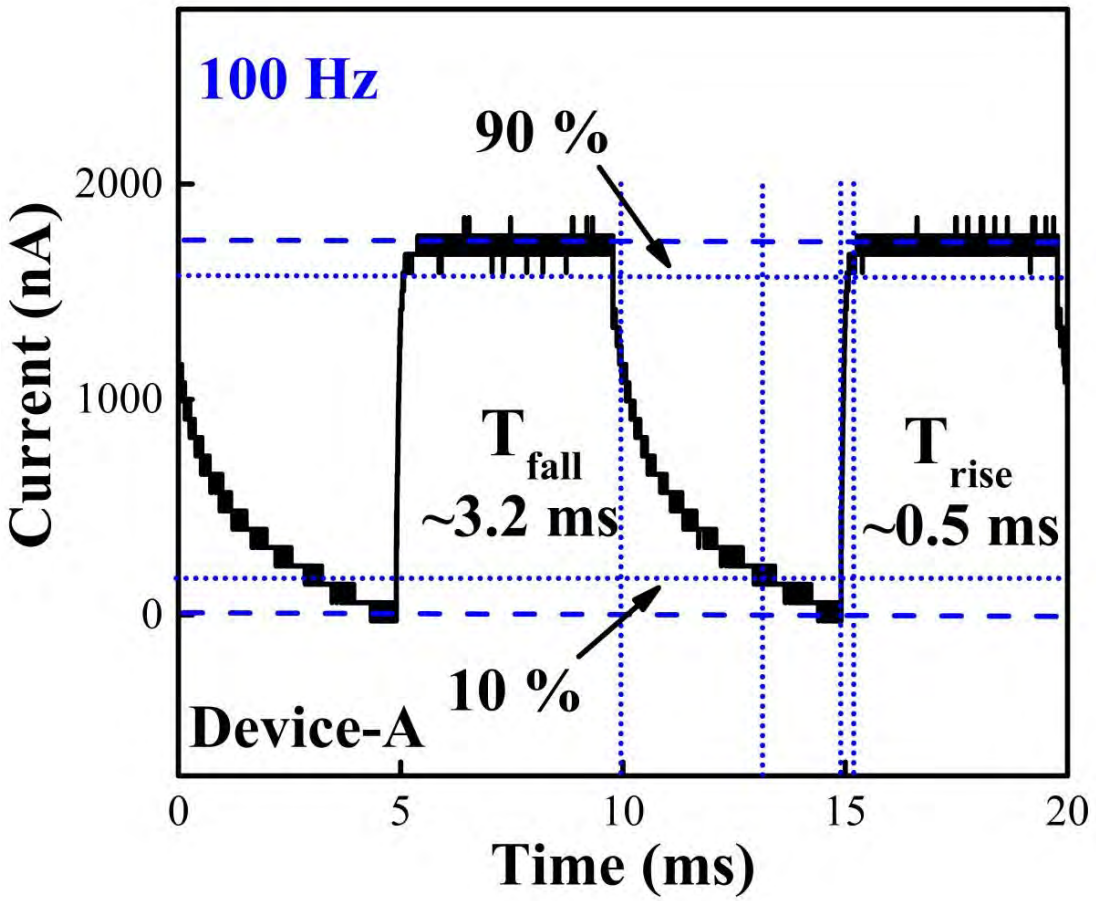

Figure S13. Waveforms of device A showing the rise and decay times upon 450 nm laser illumination at a power density of 20 mW cm^{-2} and bias of 0.5 V.

Table S1. Summary of deposition parameters

Process	Parameter	Value/Condition
NH_3 Plasma	Frequency	13.56 MHz
	Power	10 W
	Exposure Time	20 min
	NH_3 flow ratio	0-25 sccm
CVD Growth	Precursor-Substrate Distance	40 cm
	Carrier Gas (Ar)	40 sccm
	Reactive sources (CsBr, PbBr2)	0.05 g，0.05 g
	Growth Temperature	300°C
Au Electrode Deposition	Sputtering Power	30 W, 40 mA
	Sputtering time	20 min
	Gas	Ar
	pressure	4 Pa
	Substrate temperature	Room temperature

Table S2. Summary of performance parameters of photodetectors fabricated with organic, hybrid or inorganic perovskite films.

Absorbers	Detection Style	R (A W^{-1})	D* (Jones)	t_{rise}/t_{fall} (us)	Ref.
$MAPbBr_3$ film	Visible Detection	5.04	5.37×10^{12}	80/110	(3)
$MAPbI_3$ film	Visible Detection	81	$> 1\times10^{10}$	230/380	(4)
$MASnPbI_3$ film	Infrared Detection	0.2	$\sim1\times10^{12}$	2.27	(5)
$CsPbCl_3$ film	UV Detection	0.22	4.06×10^{13}	1.92/0.45	(6)
$CsPbBr_3$ nanocrystals film	Visible Detection	3	1.2×10^{13}	-	(7)
$CsPbBr_3$@SiOR nanocrystals film	Visible-UV Detection	44.5	9×10^{13}	5000/4600	(8)
$CsPbBr_3$ film	Visible Detection	3.15	3.94×10^{12}	8000/6500	(9)
$CsPbBr_3$ film	Visible Detection	55	9×10^{12}	430/318	(10)
$CsPbBr_3$ film	Visible Detection	62.7	7.7×10^{12}	100/300	This work

"–": not available

References：

[1] Rambadey, O. V.; Kumar, A.; Sati, A.; Sagdeo, P. R. Exploring the Interrelation between Urbach Energy and DielectricConstant in Hf-Substituted $BaTiO_3$, *ACS Omega* **2021**, *6*(47), 32231-32238.

[2] Cao, Y.; Zhang, X.; Zhao, K.; Wei, Y.; Zhang, L.; Zhang, H.; Wang, W.; Cui, C.; Wang, P.; Lin, P.; Wu, X.; Song, C.; Ni, Z.; Xue, J.; Wang, R.; Xu, L. In situ Crosslinked Robust Molecular Zipper at the Buried Interface for Perovskite Photovoltaics, Adv. Funct. Mater. **2025**, *35*, 2422205.

[3] Mei, L.; Zhang, K.; Cui, N.; Yu, W.; Li, Y.; Gong, K.; Li, H.; Fu, N.; Yuan, J.; Mu, H.; Huang, Z.; Xu, Z.; Lin, S.; Zhu, L. Ultraviolet-Visible-Short-Wavelength Infrared Broadband and Fast-Response Photodetectors Enabled by Individual Monocrystalline Perovskite Nanoplate. *Small* **2023**, 19 (37), 2301386.

[4] Hu, W.; Huang, W.; Yang, S.; Wang, X.; Jiang, Z.; Zhu, X.; Zhou, H.; Liu, H.; Zhang, Q.; Zhuang, X.; Yang, J.; Kim, D. H.; Pan, A. High-Performance Flexible Photodetectors Based on High-Quality Perovskite Thin Films by a Vapor–Solution Method. *Adv. Mater.* **2017**, 29 (43), 1703256.

[5] Zhu, H. L.; Lin, H.; Song, Z. L.; Wang, Z. S.; Ye, F.; Zhang, H.; Yin, W. J.; Yan, Y. F.; Choy, W. C. H. Achieving High-Quality Sn-Pb Perovskite Films on Complementary Metal-Oxide-Semiconductor-Compatible Metal/Silicon Substrates for Efficient Imaging Array. *ACS Nano* **2019**, 13 (10), 11800–11808.

[6] Zhan, X.B.; Zhang, X.N.; Liu, Z.Y.; Chen, C.; Kong, L.X.; Jiang, S.L.; Xi, S.; Liao, G.L.; Liu, X.Y. Boosting the Performance of Self-Powered $CsPbCl_3$-Based UV Photodetectors by a Sequential Vapor-Deposition Strategy and Heterojunction Engineering. *ACS Appl. Mater. Interfaces* **2021**, 13 (38), 45744–45757.

[7] Duong, T. T.; Tran, P. N.; Van, T. P.; Nguyen, D. H.; Tran, V. D. A Dense, Pinholes-Free Pure Cubic Phase $CsPbBr_3$ Nanocrystals Film for High-Performance Photodetector. *Electron. Mater. Lett.* **2024**, 20, 217–223.

[8] Ely, F.; Vieira, K. O.; Reyes-Banda, M. G.; Quevedo-Lopez, M. Broadband Photodetectors from Silane-Passivated $CsPbBr_3$ Nanocrystals by Ultrasound-Mediated Synthesis. *Nanoscale* **2024**, 16, 10833–10840.

[9] Wu, W.; Han, X.; Li, J.; Wang, X.; Zhang, Y.; Huo, Z.; Chen, Q.; Sun, X.; Xu, Z.; Tan, Y.; Pan, C.; Pan, A. Ultrathin and Conformable Lead Halide Perovskite Photodetector Arrays for Potential Application in Retina-Like Vision Sensing. Adv. Mater. 2021, 33 (9), 2006006.

[10]Li, Y.; Shi, Z.; Li, S.; Lei, L.; Ji, H.; Wu, D.; Xu, T.; Tian, Y.; Li, X. High-Performance Perovskite Photodetectors Based on Solution-Processed All-Inorganic $CsPbBr_3$ Thin Films. *J. Mater. Chem. C* **2017**, 5, 8355-8360.